

Visualization of Fluid Flows in Virtual Environments

Ziegeler, S. B. ¹⁾, Gopal, G. P. ¹⁾, Blades, E. ²⁾, Moorhead, R. J. ¹⁾, Marcum, D. L. ²⁾ and Guan, Y. ¹⁾

1) ERC GRI Visualization, Analysis and Imaging Laboratory, Mississippi State University, MS, U.S.A.

E-mail : {sean | gopi | rjm | guanyl } @gri.msstate.edu

2) ERC SimCenter, Mississippi State University, MS, U.S.A.,

E-mail : { blades | marcum } @simcenter.msstate.edu

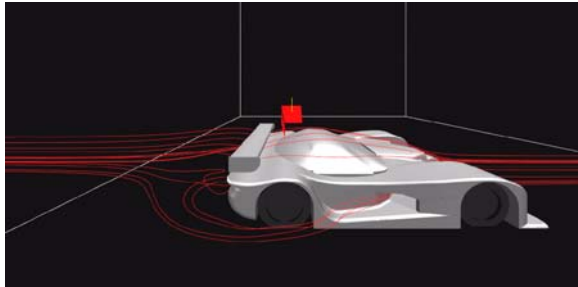


Fig. 1. Virtual Environment (VE) simulator side view of stream lines about a GT race car model

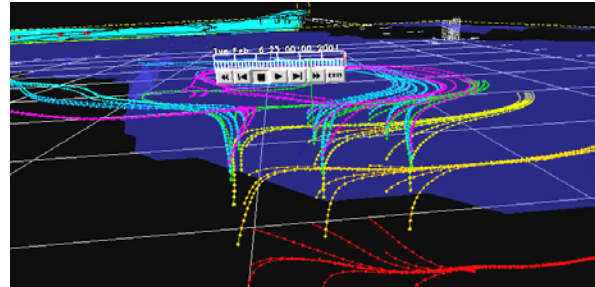


Fig. 2. VE simulator view of path lines computed with six days of oceanographic flow data



Fig. 3. Full VE view of an atmospheric simulation of a large snow and ice storm



Fig. 4. Full VE view of oceanographic and atmospheric flow data visualized simultaneously

Virtual Environments (VE's) provide advantages over conventional displays for fluid flow analysis. The stream lines for the GT Race Car (Fig. 1) are pre-computed by a flow-solver using a large volumetric model. The oceanographic flow data is model-generated and visualized by our VE software, *Triton II* (Fig. 2). These top two figures illustrate VE simulators for conventional displays. Certain atmospheric models predict the development and movement of water particles for storms (Fig. 3), while newer systems simultaneously run oceanographic and atmospheric models utilizing each other's boundary conditions (Fig. 4). The last two figures exemplify VE visualization hardware to show how the superior view can provide improved analysis.

Flow Visualization of Coaxial Jet Excited with Varying Phase Differences

Kiwata, T.¹⁾ and Okajima, A.¹⁾

1) Department of Mechanical Systems Engineering, Kanazawa University, 2-40-20 Kodatsuno, Kanazawa, 920-8667, Japan

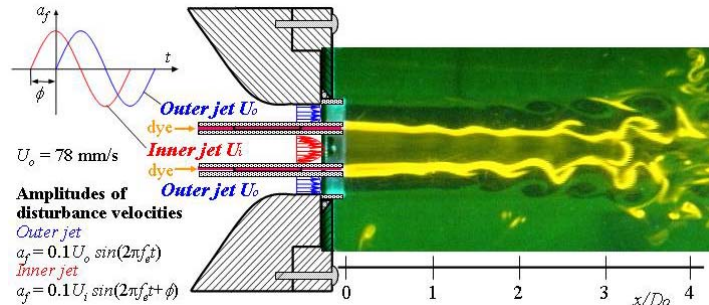


Fig. 1. Flow pattern of the unexcited jet at the mean inner circular jet velocity, U_i , to the mean outer annular jet velocity, U_o , ratio = 0.6. Initial vortex frequency of the unexcited jet in the mixing layer is $f_n = 2.96\text{Hz}$ and Reynolds number is 3000

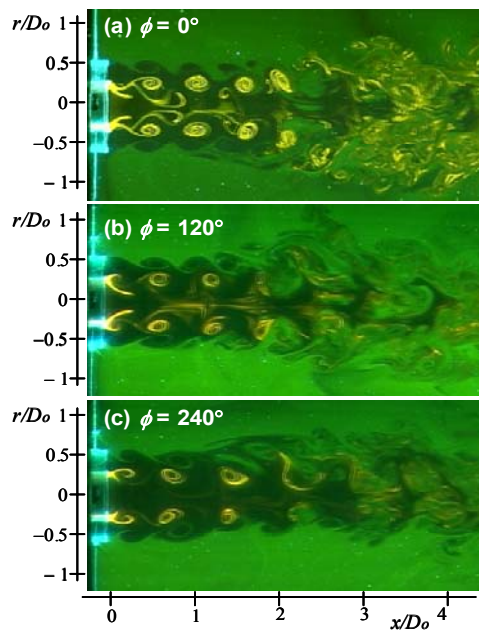


Fig. 2. The frequencies of the excitation f_e and the initial vortex f_n are matched. Here, ϕ is the phase angle difference between the outer and the inner jet perturbations

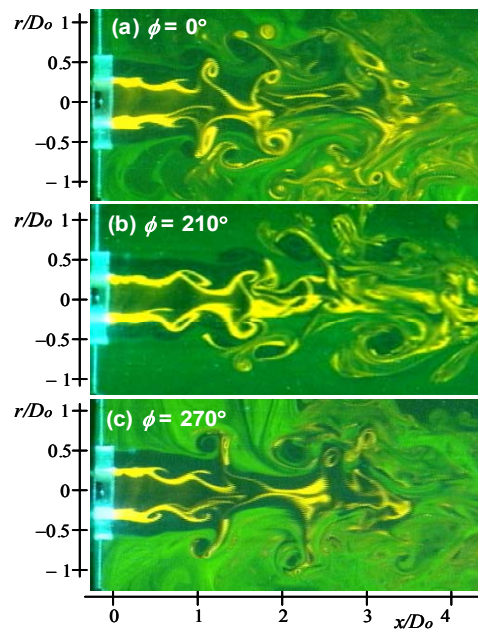


Fig. 3. Dye visualization indicates the effect of the phase angle difference on the development of the flow structure for the excitation frequency ratio $f_e/f_n = 0.5$

The vortical structures of the excited coaxial jet are visualized by using a laser-induced fluorescence technique. The forced excitations with various phase angle differences ϕ have slight effects on the vortex pattern of the shear-layer in Fig. 2. The center-line velocity increases more than the unexcited jet in all Figures. Vortex-pairing phenomena are performed dominantly in Fig. 3. The merged vortices are convected towards to the downstream without further vortex-pairing in Fig. 3(b). The outer and inner vortices of shear-layer are rolled up each other in the radial direction, and also the width of jet in the near region of the nozzle exit is increased in Fig. 3(c).

Electrical Capacitance Tomography Imaging of Gas-Solid and Gas-Liquid-Solid Fluidized Bed Systems

Fan, L. -S.¹⁾, W. Warsito.¹⁾ and B. Du.¹⁾

1) Department of Chemical Engineering, The Ohio State University, 140 West 19th Avenue, Columbus, OH 43210-1180, U.S.A.

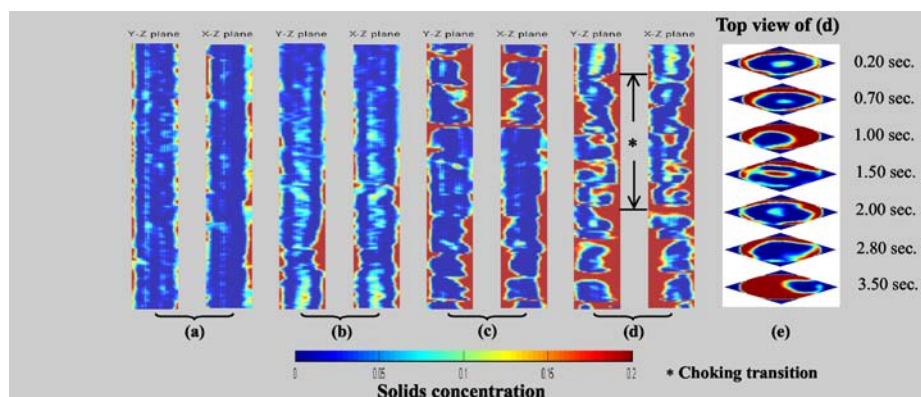


Fig. 1. Instantaneous solids concentration distributions of a circulating fluidized bed (CFB) with Group B particles at $U_g = 2.4$ m/s ($G_s = 8.57$ kg/m²s (a); 11.43 kg/m²s (b); 25.72 kg/m²s (c); 14.86 kg/m²s (d), (e))

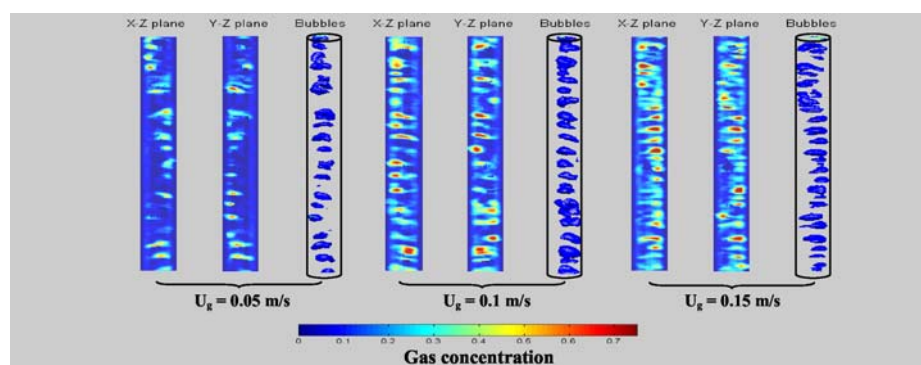


Fig. 2. Instantaneous gas concentration distributions of a gas-liquid-solid fluidized bed

The electrical capacitance tomography (ECT) based on the neural network multi-criteria optimization image reconstruction technique (NNMOIRT) developed by this research group (US Patent # 6577700 B1) is used to accurately reveal the instantaneous phase holdup distribution of complex multiphase flow systems. Figures 1 and 2 show the time series of ECT images in a given plane of the column; the images stack up to reflect the dynamic behavior of the phase holdup distribution. Specifically, Fig. 1 shows the real time solids concentration distribution variation for a 0.1-m ID and 6.32-m-high CFB riser (0.5 m above the distributor) with coarse sand particles as fluidized material ($d_p = 240$ μm and $\rho_p = 2200$ kg/m³) for a gas velocity of 2.4 m/s. With an increase in the solids circulation rate, G_s , the CFB riser undergoes a variation from the double solids-ring flow structure (a), three-region flow structure (b), to slug flow structure (c). Figure 1 (d) and (e) illustrate the dynamic process of the choking transition. Figure 2 shows the real time gas concentration distributions at a level 0.2 m above the distributor in a gas-liquid-solid fluidized bed under different gas velocities and without liquid inlet flow. Air, Norpar 15 ($\rho = 773$ kg/m³) and glass beads ($d_p = 200$ μm , $\rho_p = 2470$ kg/m³) are used as gas, liquid and solid phases, respectively. Spiral motion of bubbles is clearly observed at a low gas velocity.

Visualization of Turbulence Structures Reorganization in Thermal Convection Subjected to External Magnetic Field

S. Kenjeres.¹⁾ and K. Hanjalic.¹⁾

1) Department of Multi Scale Physics, Faculty of Applied Sciences, Delft University of Technology, Lorentzweg 1, 2628 CJ Delft, The Netherlands

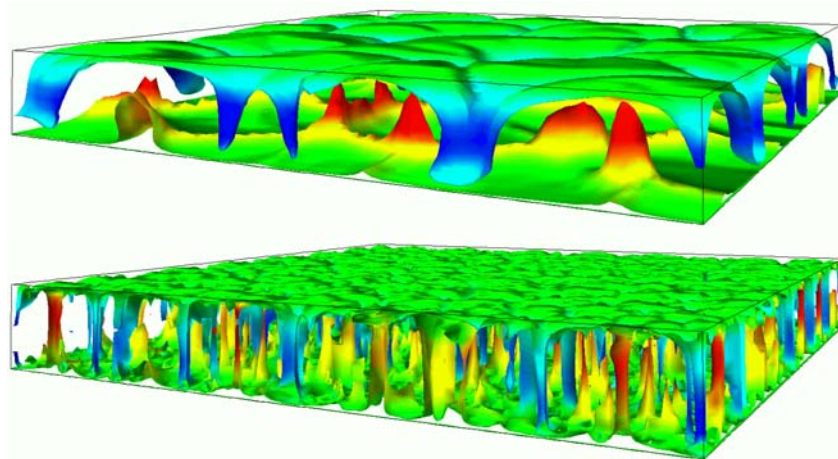


Fig. 1. Spatial reorganization of thermal plumes (isosurfaces of temperature, $T_{\text{ref}}+0.1\Delta T$ and $T_{\text{ref}}-0.1\Delta T$, colored by vertical velocity, $-0.3 < W < 0.3$) in magnetic Rayleigh-Benard convection: $Ra=10^7$, $Ha=0, 100$; Homogeneous magnetic field is applied in the vertical direction, $B(0,0,B_z)$

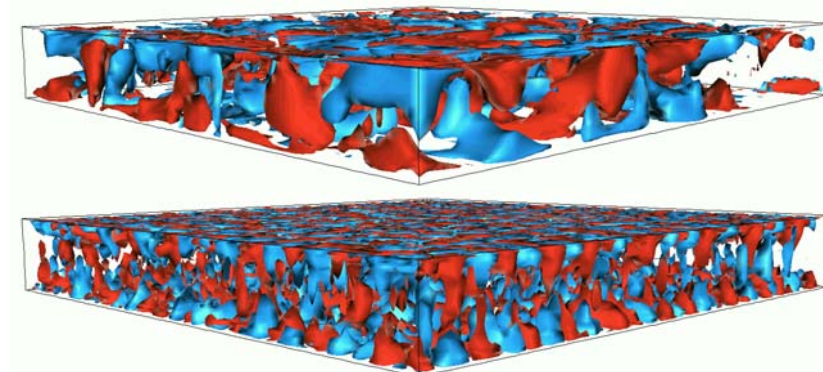


Fig. 2. Vertical vorticity component, $\omega_z = \omega_z / |\omega| = 0.6$ (blue) and -0.6 (red) for $Ha=0$ (above) and $\omega_z = \omega_z / |\omega| = 0.3$ (blue) and -0.3 (red) for $Ha=100$

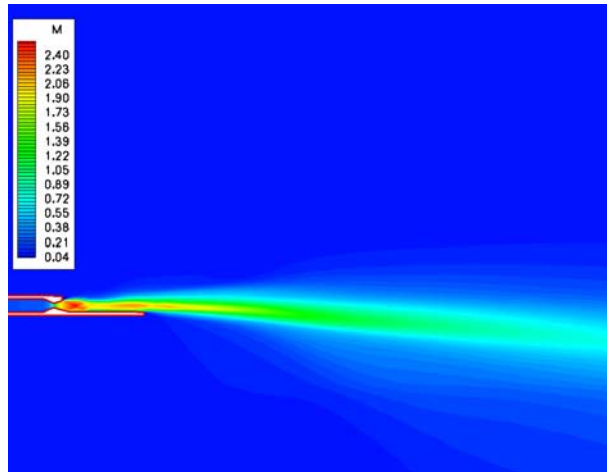
Numerical simulations of classic and magnetic turbulent thermal convection between two infinite horizontal walls of different temperatures have been performed using the transient Reynolds averaged Navier-Stokes (T-RANS) method. A major effect of vertically oriented magnetic field is in the suppression of the velocity and vorticity components in the horizontal plane (i.e. the plane where the Lorentz force is active). This suppression leads to an alignment of the velocity vector with magnetic field deforming the convective roll/cells into vertically oriented cylindrical structures.

Mach Number Distribution and Plume Direction Prediction of a Rocket Thruster Operating at Four Different Combustion Chamber Pressures

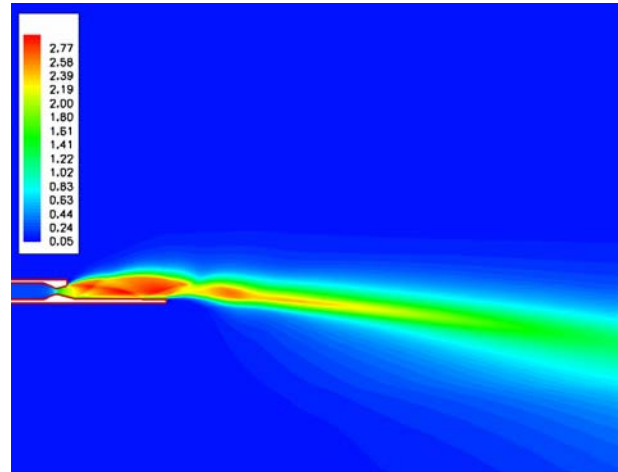
Farhad Davoudzadeh¹⁾ and Nan-Suey Liu¹⁾

1) NASA Glenn Research Center, MS 5-10, 21000 Brookpark Rd., Cleveland, OH 44135-3191, U.S.A.

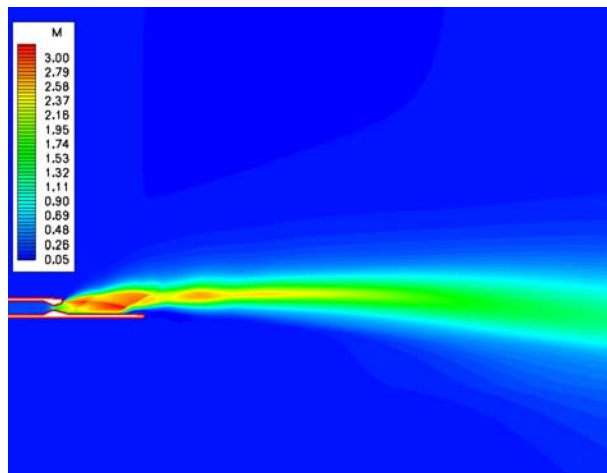
E-mail : Farhad.Davoudzadeh@grc.nasa.gov, Nan-Suey.Liu-1@nasa.gov



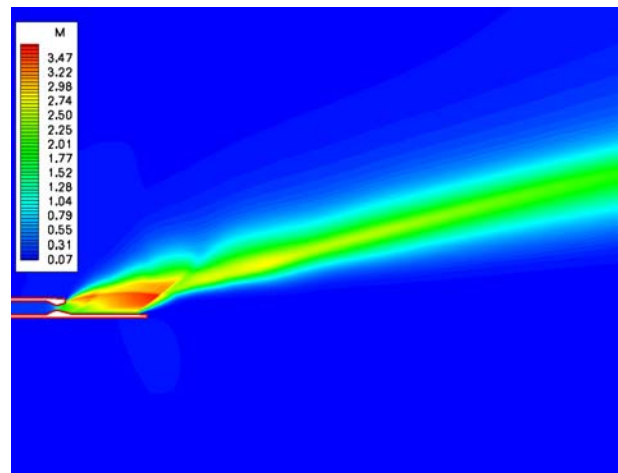
(a) Chamber Pressure = 130 psia



(b) Chamber Pressure = 250 psia



(c) Chamber Pressure = 300 psia



(d) Chamber Pressure = 500 psia

Navier-Stokes numerical simulations showing the supersonic flow field induced by a H₂-O₂ rocket thruster with an attached panel, under a variety of operating conditions. The plume direction is controlled by the shocks. It moves from a straight and slightly downward direction to an upward direction as the combustion chamber pressure is increased from 130psia to 500psia. The 500psia case exhibits the highest plume angle, where the Mach number remains very high past the initial shock, aft of the inclined ramp, and over the flat panel.

Ferrohydrodynamic Instabilities in DC Magnetic Fields

Rinaldi, C.¹⁾ and Zahn, M.²⁾

1) Department of Chemical Engineering, University of Puerto Rico at Mayagüez, Mayagüez, PR, U.S.A.

2) Department of Electrical Engineering and Computer Science and Laboratory for Electromagnetic and Electronic Systems, Massachusetts Institute of Technology, Cambridge, MA, U.S.A.



Ferrofluid instabilities in DC magnetic fields for an Isopar-M based ferrofluid with saturation magnetization of about 400 Gauss. a) 1200 Gauss 5 mm diameter magnet behind small ferrofluid droplet surrounded by propanol to prevent ferrofluid wetting of 1 mm gap glass plates; Peak pattern with magnetic field perpendicular to ferrofluid layer. The peaks initiate in a hexagonal array when the magnetic surface force exceeds the stabilizing effects of fluid weight and surface tension – b) 200 Gauss, c) 330 Gauss, d) 400 Gauss; e), f) Labyrinth instability with ferrofluid between 1 mm gap glass plates in 250 Gauss vertical magnetic field.